Supporting Information

An operando spectroscopic examination of the influence of trace humidity on interdigital back contact metal halide perovskite solar cells

Mehmet E. Bayat,*[ab] Edgar R. Nandayapa,[c] Carlo Tiebe,[a] Eva L. Unger[cd] and Emil J. W. List-Kratochvil*[ef]

a. Bundesanstalt für Materialforschung und -prüfung (BAM), Richard-Willstätter-Str. 11, 12200 Berlin, Germany. E-mail: mehmet-emin.bayat@bam.de
b. Department of Chemistry and Biology, and Center of Micro- and Nanochemistry and (Bio-)Technology (Cμ), University of Siegen, Adolf-Reichwein-Str. 2, 57068 Siegen, Germany
c. Helmholtz Zentrum Berlin für Materialien und Energie, HySPRINT Innovation Lab, Kekulestrasse 5, 12489 Berlin, Germany
d. Department of Chemistry, Center for the Science of Materials Berlin, Humboldt Universität zu Berlin, Zum Großen Windkanal 2, 12489 Berlin, Germany
e. Helmholtz-Zentrum Berlin für Materialien und Energie, Brook-Taylor-Straße 6, 12489 Berlin, Germany
f. Department of Physics, Department of Chemistry, Center for the Science of Materials Berlin, Humboldt Universität zu Berlin, Zum Großen Windkanal 2, 12489, Germany. E-Mail: emil.list-kratochvil@hu-berlin.de

1. Device preparation

a)

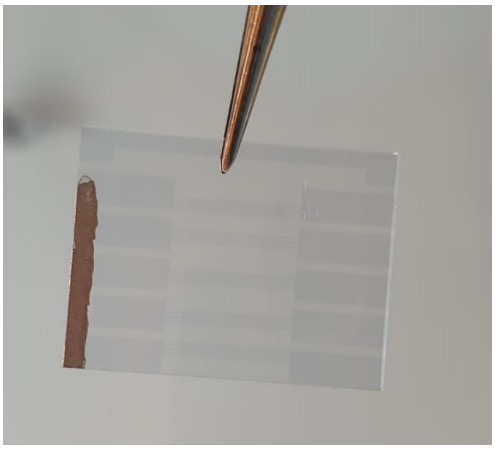

b)

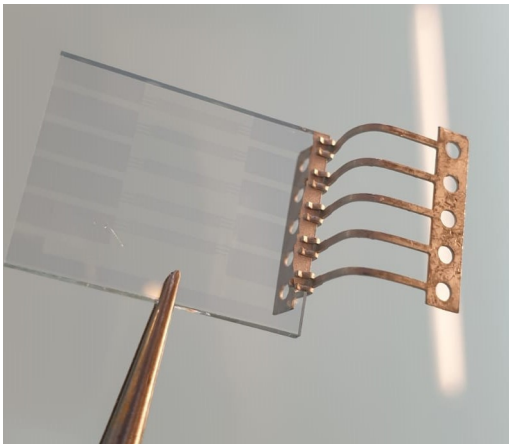

Figure S1: Preparation of the substrate for the electrochemical deposition. In a) the coating of the electrically conductive adhesive on the electrodes to be deposited with the selective layer and in b) with bent connection legs for a proper electrical connection.

a)

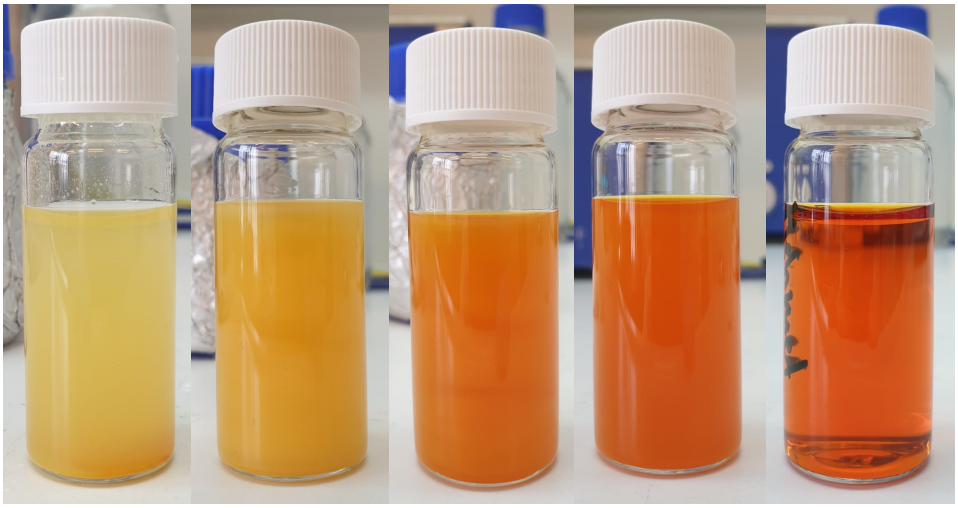

b) c)

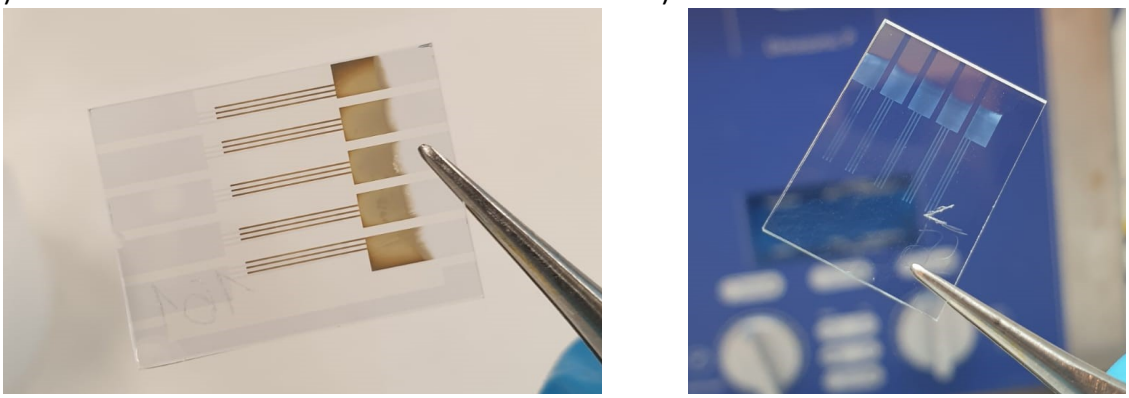

Figure S2: a) Development of the peroxo-titanium stock solution to complete clarity, with each photo taken at 7-minute intervals. In b) the brown titanium oxide species freshly deposited on the electrodes, and in c) after annealing, converting it to a transparent, bluish shimmering layer strongly bound to the ITO.

a) b)

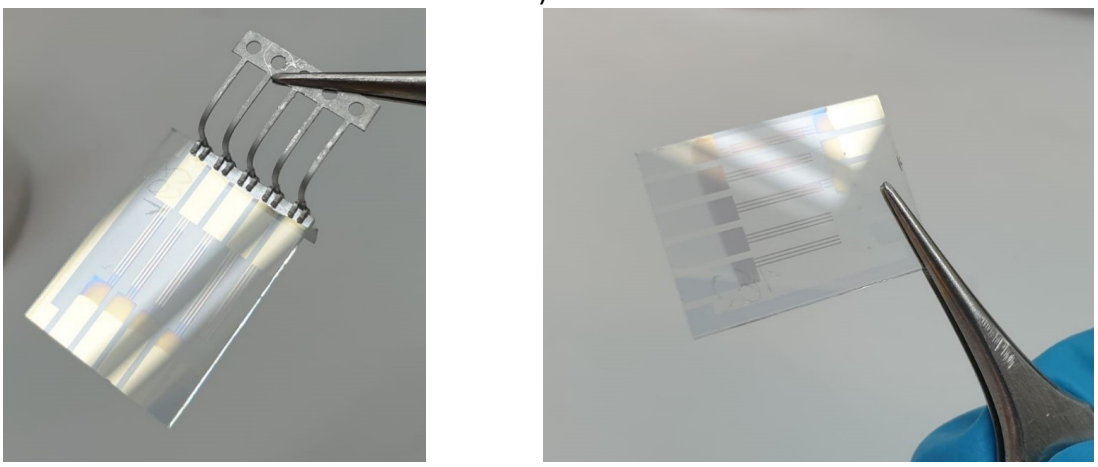

Figure S3: Preparation of the substrate for the electrochemical deposition of PEDOT. In a) the prepared substrate with conductive adhesive and connection leg on the electrode side on which PEDOT has to be deposited, while titanium dioxide has already been deposited on the other electrode side. In b) the substrate after PEDOT deposition, so that a complete substrate with deposited selective layers (TiO_2 & PEDOT) has been obtained.

a) b)

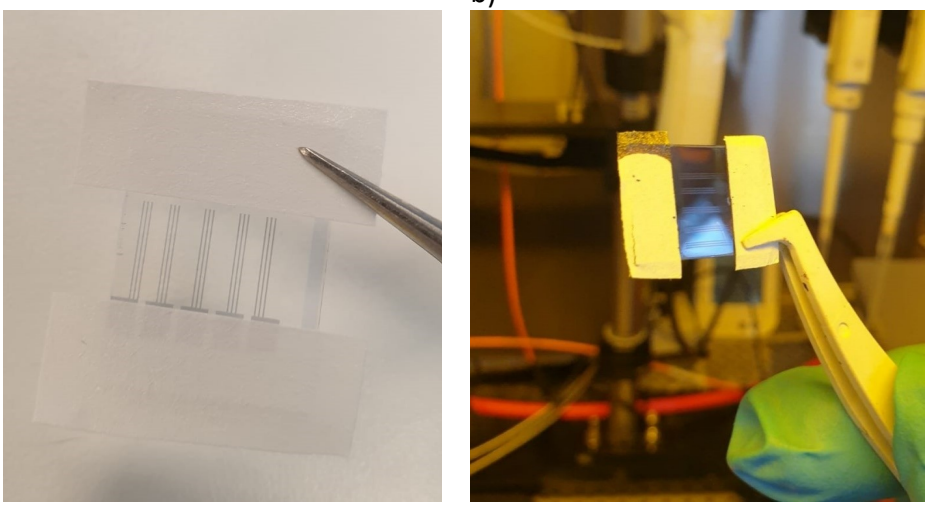

Figure S4: a) A prepared substrate with PEDOT and TiO_2 with crepe tape for MHP deposition. b) A fully functional IBC solar cell directly after MHP annealing for 45 min at 100 °C.

2. Experimental setup

a)

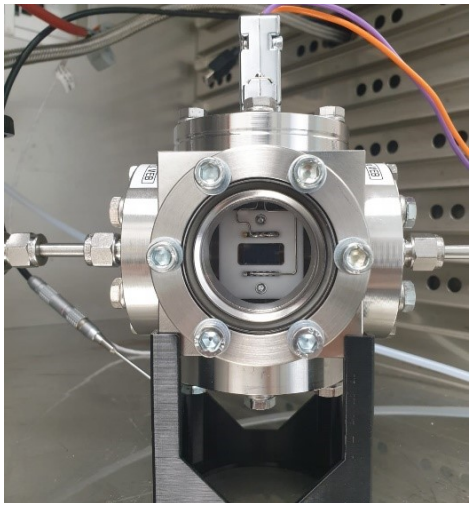

b)

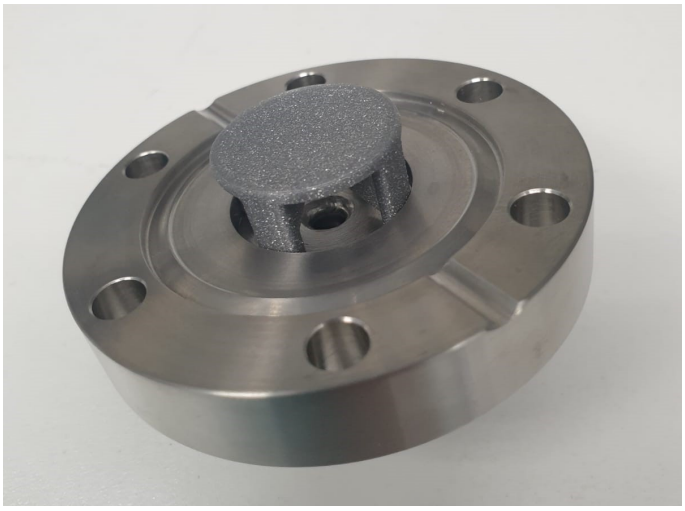

c)

d)

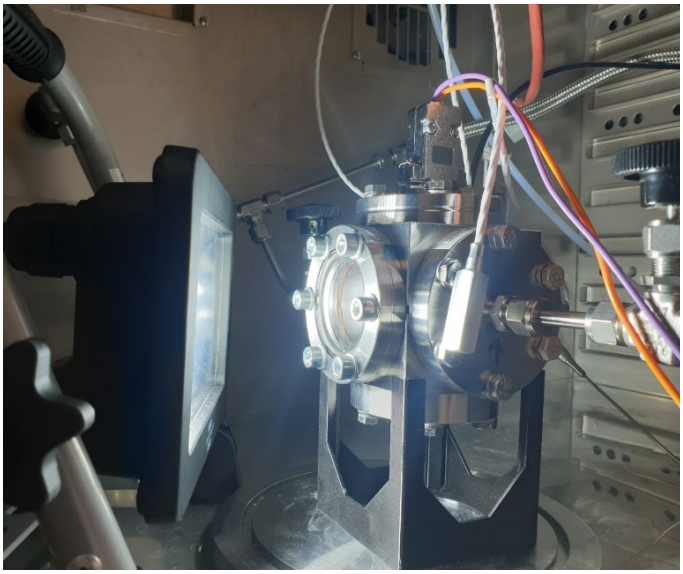

Figure S5: a) The measuring cell fully equipped with a clear view inside. b) A 3D printed flow conditioner equipped on the gas inlet to transfer the laminar flow into a turbulent flow for better mixing and faster response times.

c) The IBC sample holder. The electrical connection out of the measuring cell was provided by a flange with a welded-in DSUB-D9 connector. The electrical connection from the sample holder to the IBC solar cell was ensured by pins with spring contact. d) The measuring cell equipped with an IBC solar cell under illumination.

The outlet of the gas mixing system was connected to the measuring cell using Swagelok stainless steel titanium alloyed tubing (product number: 316TI-T6M-S-1.0M-6ME). The measuring cell itself consisted of a stainless-steel CF Cube (Vacom, CUBE40-304, product number: 300454) fitted with six CF flanges DN40 (Vacom, F40-304, product number: 300800), shown in **Figure S5a**. Among these flanges, two were modified with a stainless-steel Swagelok 6 mm tube fitting (product number: SS-6M0-1-4RT) for the gas inlet and outlet. To promote better mixing, a 3D-printed flow conditioner was fitted to the gas inlet to convert the laminar flow into turbulent flow within the measuring cell, shown in **Figure S5b**. Additionally, a flange made of steel with a borosilicate viewport (Vacom, VPCF40B-L, product number: 303142) was mounted to permit light transmission into the measuring cell. Two blind flanges were installed on the unused connectors of the CF-Cube. The last steel flange was modified to fit a sample holder specifically designed for the IBC solar cell, shown in **Figure S5c**. It was engineered so that the IBC solar cell was placed exactly in the centre of the viewport while providing a gas-tight connection to the source measure unit. To ensure proper sealing of the measuring cell, copper gaskets (Vacom, CUA40, product number: 300440) were used, except for the flange with the sample holder. Since this flange had to be disassembled and reassembled regularly, a fluorocarbon rubber gasket was used here (Vacom, VGF40, product number: 303064). Further, a Brennstuhl EL 2050 M spotlight was attached in front of the viewport flange to provide a light resource, shown in **Figure S5d**. The measuring cell and the LED spotlight were set up in a WTC Binder temperature chamber to generate stable ambient conditions (setpoint of 20 °C). The spotlight is heating the CF cube, while the temperature chamber is counteracting, resulting in a total heating of the measuring cell of around 1 °C. To operate the transfer standard dew point hygrometer at the required specifications, a bypass using a tee fitting and two ball valves was installed to regulate the flow rate within a range of 1700 mL_n/min.

Given that the LED spotlight used at the trace humidity test bench was not a sunlight simulator (SuSi), it is crucial to address the issue of comparability between the spotlight and a standardized sunlight simulator that generates 1 according to AM1.5G standard. An exact lamp comparison was not necessary. Rather, it was important to investigate how high the

irradiance deviation was at the respective measurement location of the glove box and of the measuring cell. For this a Thorlabs PM100A power meter with a S120VC sensor was used to measure the level of irradiance. The power meter was able to quantify the irradiance in relation to the following wavelengths: 800 nm, 750 nm, 636 nm, 561 nm, 530 nm, 440 nm, 400 nm, 390 nm, and 200 nm. The measurement in the glove box was conducted with an irradiance set point of 1 sun under AM1.5G standard. Subsequently, the irradiance of the EL 2050 M lamp was determined. For this purpose, the lamp was first brought into thermal equilibrium by operating it for one hour at a temperature chamber set point of 20.0 °C. The power meter sensor was mounted into the measuring cell at the location of the IBC solar cell. The lamp was positioned in the same way as for all trace humidity measurements carried out. The measurement results are shown in **Figure S6**. A comparison of the measured values shows that the lamps deliver very similar results to each other regarding the corresponding wavelength examined. This observation suggests that the illumination conditions at both measurement setups exhibit a good degree of similarity.

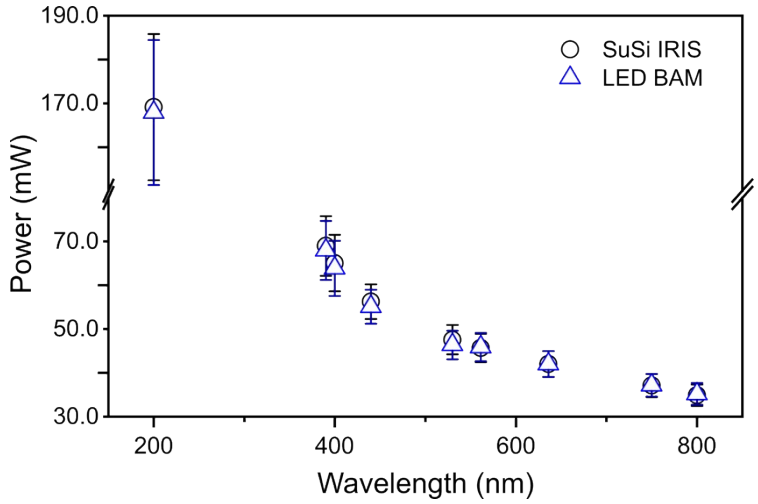

Figure S6: Comparison of the power output of the used lamps. In red the power output of the spotlight (EL 2050 M) and in black the power output of the reference solar simulator at 1 sun and AM1.5G standard.

2. Layer characterization and device topography

2.1. Titanium dioxide

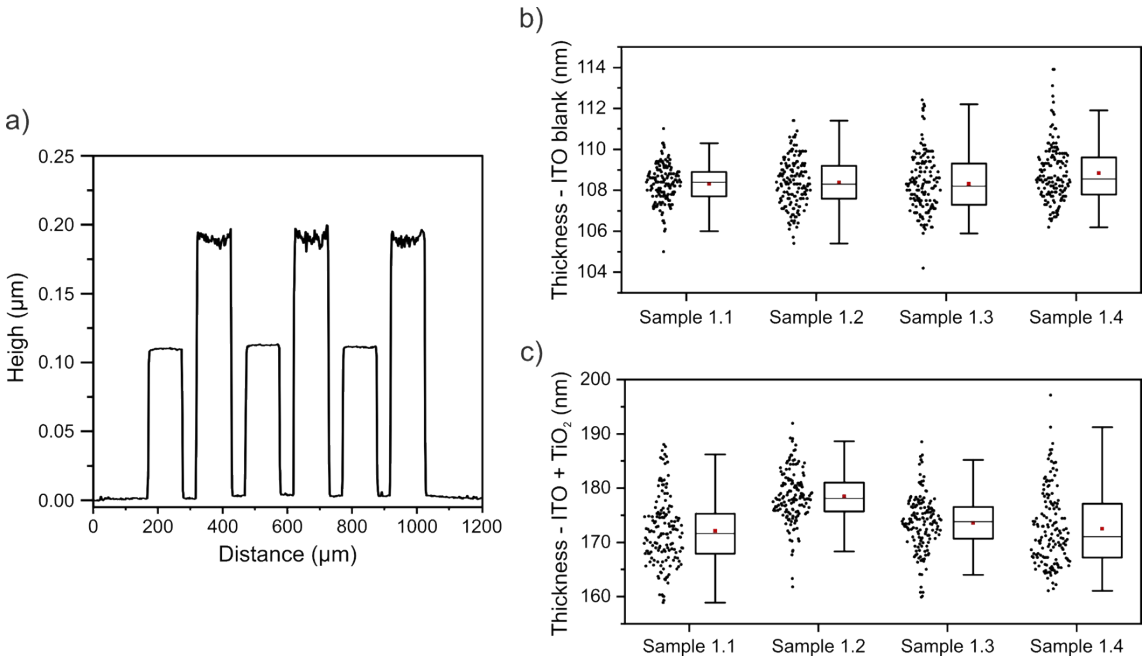

Figure S7: Measured thickness of the deposited TiO_2 layer. a) A measured profile of deposited TiO_2 on the interdigital interface. b) The layer thickness of the blank ITO electrodes. c) The layer thickness of TiO_2 on ITO. The mean layer thickness of TiO_2 on ITO was 66 nm ± 14 nm.

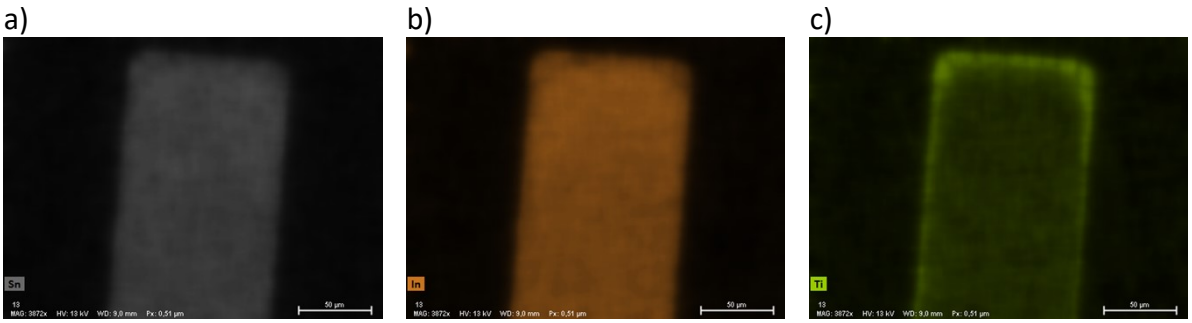

Figure S8: EDX mapping of an ITO electrode deposited with TiO_2. In a) for tin, b) for indium and c) for titanium.

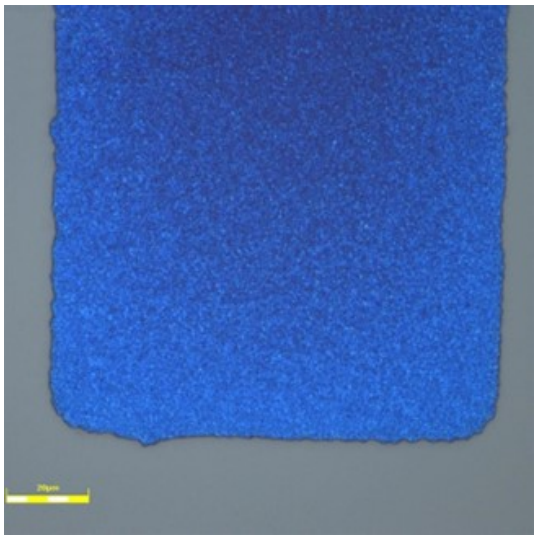

Figure S9: Light microscope image of an electrode tip coated with TiO_2 (the scale in 20 µm).

2.2. PEDOT

Figure S10a shows a profile of the deposited PEDOT on the investigated ITO substrates. The mean layer thickness of the ITO on the investigated samples (of two batches) was 111.0 nm ± 2.0 nm, and the mean layer thickness of PEDOT on ITO was 148.1 nm ± 5.5 nm. It should be noted that the PEDOT layer formed sharp edges that grew into the deposition bath due to the well-known phenomenon of current concentration at sharp edges. This concentration occurs because the current flows preferentially in regions with higher electric fields. The plateaus between the spikes were used to evaluate the PEDOT layer thickness. It results a mean layer thickness of 37.0 nm ± 7.5 nm for PEDOT.

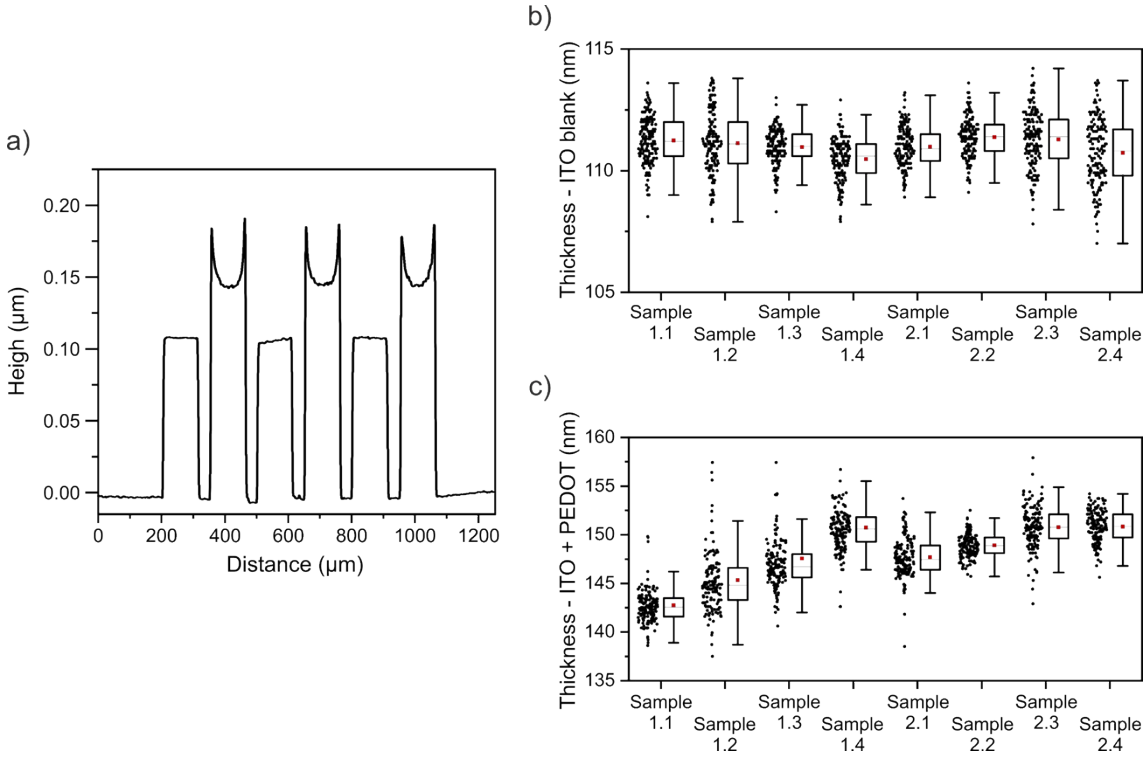

Figure S10: Measured thickness of the deposited PEDOT layer. a) A measured profile of the deposited PEDOT. b) The layer thickness of the blank ITO electrodes investigated. c) The layer thickness of PEDOT on ITO.

The ionization energy of the PEDOT:ClO_4 was determined to be (4.95 ± 0.17) eV using photoelectron yield spectroscopy, shown in **Figure S11**.

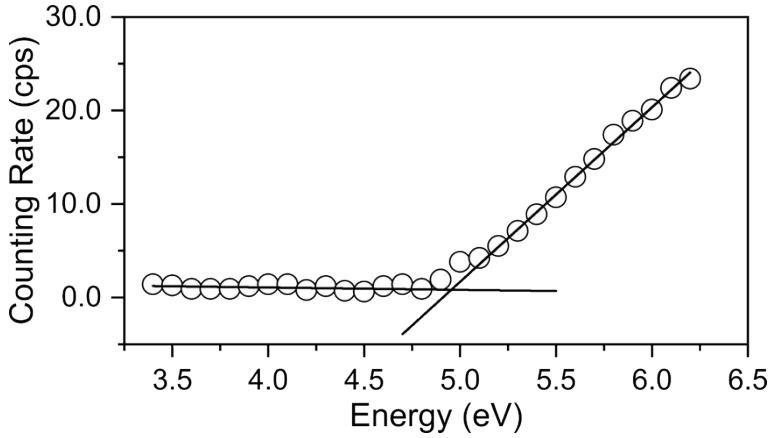

Figure S11: Measurement of the ionization energy for the PEDOT:ClO_4 on ITO using photoelectron yield spectroscopy.

a) b) c)

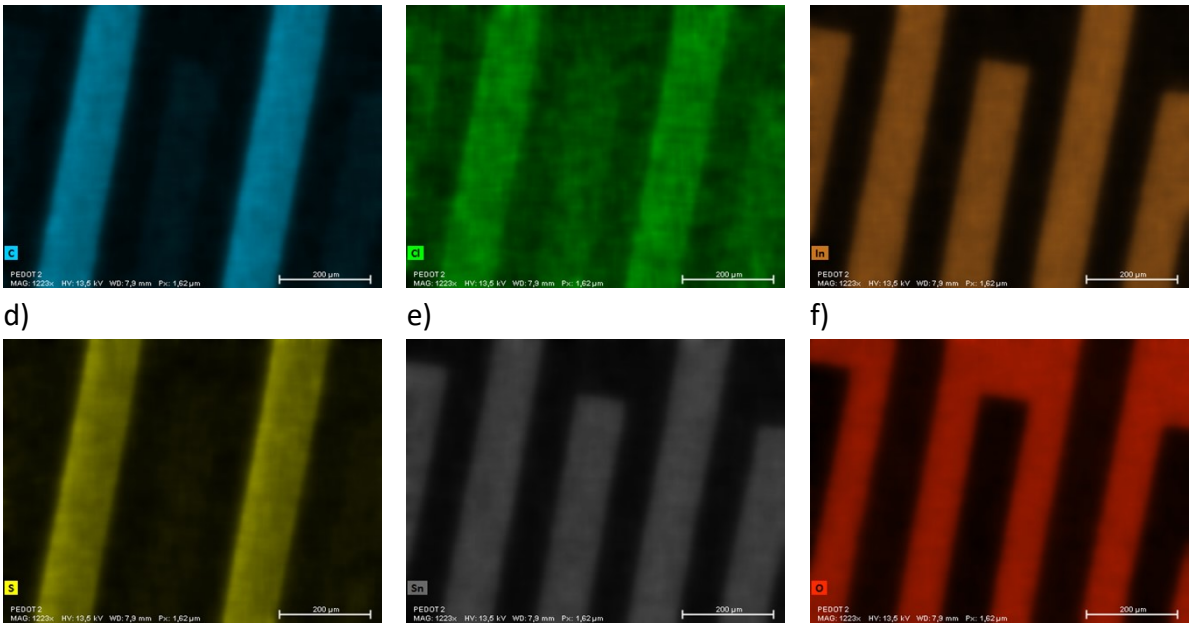

Figure S12: EDX mapping of an ITO substrate deposited with PEDOT. In a) for carbon, b) for chlorine, c) for indium, d) for sulphur, e) for tin and f) for oxygen.

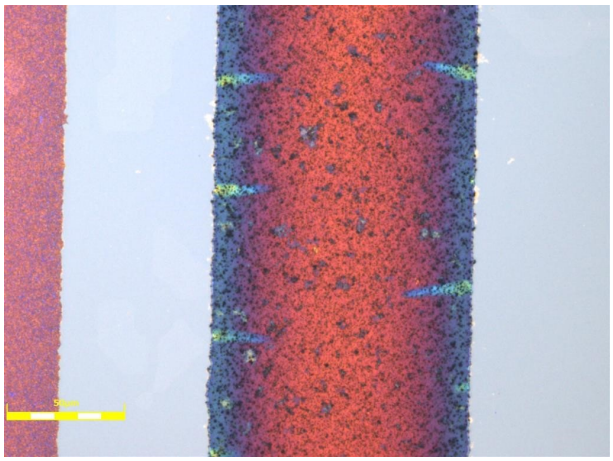

Figure S13: Light microscope image of the PEDOT on ITO, showing an uneven transmission (sharp edges) with a rough surface (the scalebar is 50 µm).

2.3. Metal halide perovskite and device topography

The layer thickness of the MHP was examined at two different positions by scratching the layer, shown in **Figure S14a**. The first position was the MHP layer thickness in the interdigital area, between the electrodes, depicted in **Figure S14b**. The second position was the MHP layer thickness far outside the interdigital area, directly on the glass, shown in **Figure S14c**. A total of 8 samples were analysed, all independently prepared from different batches. The MHP layer thickness on the glass was determined with 254.2 nm ± 35.5 nm in average. The MHP layer thickness between the interdigitated electrodes was determined with 237.1 nm ±

44.5 nm in average. No significant variations were observed, indicating that the MHP layer thickness outside and inside the interdigitated area is homogeneously distributed.

Therefore, this consistency enables a clear interpretation of the MHP topographical profile, as shown in **Figure S15a**, which was measured directly within the interdigital electrode area of an IBC solar cell. Consequently, the device topography of the interlayers could be accurately reconstructed, as illustrated in **Figure S15b**. Clear imprints were accurately measured on the surface of the MHP. Additionally, it is straightforward to associate each imprint with its corresponding selective layer, as the PEDOT spikes are distinctly visible. The topography of the MHP layer was surprising, as we did not anticipate such clear distinctions. However, it was observed that the spin-coated layers were less uniform than expected, suggesting that spin-coating may not be the optimal method for applying the MHP to this type of device architecture. Nonetheless, the layer uniformity was adequate for our application. Nevertheless, we would like to highlight this finding as it could be valuable for optimizing back-contacted solar cells in general.

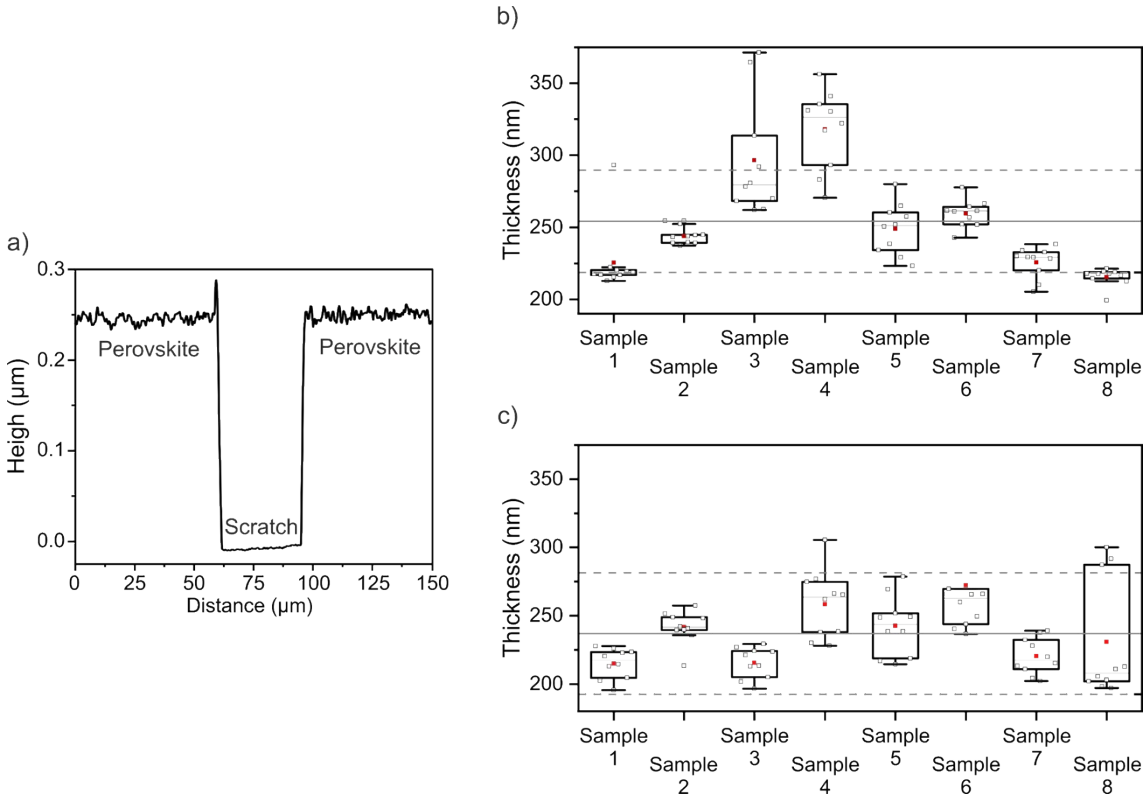

Figure S14: a) A profile of a scratch to determine the layer thickness of the MHP. b) Measured MPH layer thicknesses between the interdigitated electrodes. c) Measured MHP layer thicknesses outside of the interdigital area, on the glass.

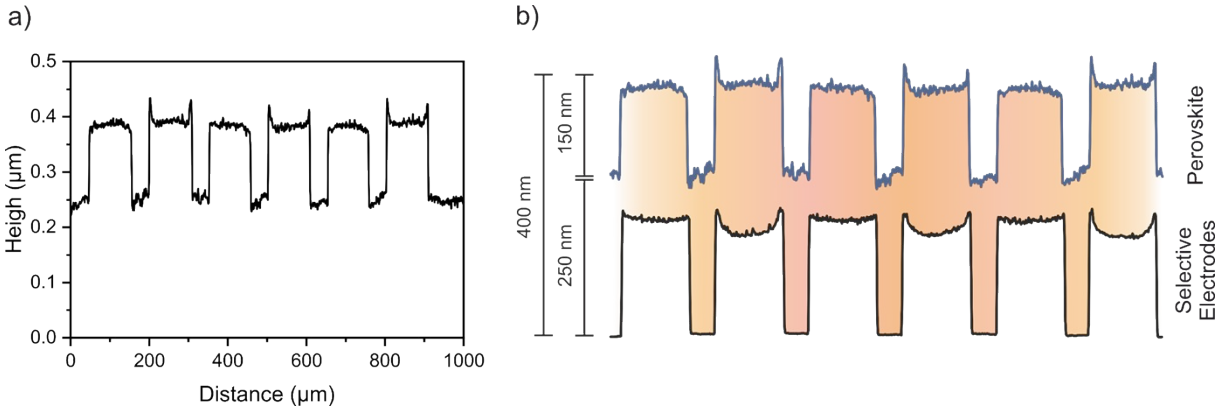

Figure S15: a) A profile of the MHP surface on an interdigitated area of an IBC solar cell. b) Observed total layer architecture of the IBC solar cells.

3. IBC solar cells – basic characterization

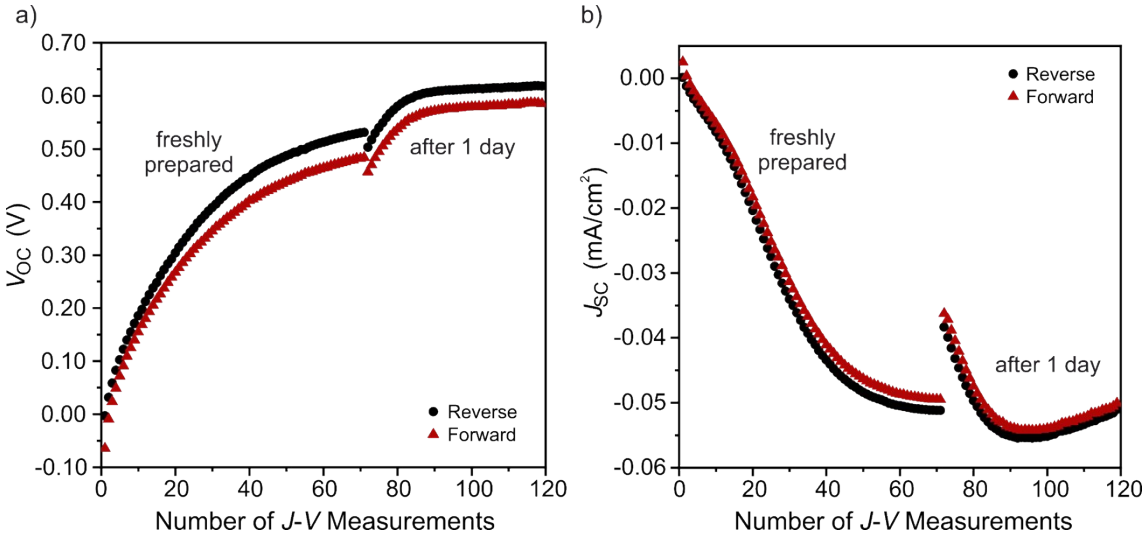

Figure S16: J-V measurements of the MHP-based IBC device for increasing voltages (forward) and decreasing voltages (reverse). In a) are the V_{OC} values and in b) the J_{SC} values presented. After approx. 95 J-V measurements, the device shows significant degradation behavior.

Figure S16 presents typical J-V characteristics as a function of conducted J-V measurements of an IBC solar cell, illustrating the gradually increase in photocurrent and photovoltage with each J-V measurement. Cycles 1 to 70 demonstrate the initial performance characteristics immediately following device preparation. Cycles 71 to 120 reflect the re-evaluated characteristics of the same device after completing the first 70 J-V measurements and a subsequent 24-hour storage period in a nitrogen-filled glovebox. The results show an irreversible enhancement in both photocurrent and photovoltage, indicating an overall improvement in performance. However, it is also evident that the photocurrent reached a

turning point, indicating that degradation mechanisms have become dominant in the device physics.

The preconditioning procedure of the IBC devices to build up photocurrent and photovoltage was performed in dry nitrogen until the V_{OC} values reached a stabilized state, as shown in **Figure S16a** (cycles 90 - 120). Experiments in trace humidified nitrogen were conducted once this condition was achieved.

4. Water outgassing

Trace humidity measurements with a dew point hygrometer are performed by measuring a condensation point at which the condensed phase (liquid water or ice) is in thermodynamic equilibrium with its surrounding gas phase. This condensation temperature is directly proportional to the water vapor partial pressure. The measurement of condensation temperatures for water vapor partial pressures below 0.20 Pa indicates frost point temperatures well below −71 °C. At such low temperatures, the amount of condensable water is quite low, and the time required to accumulate a measurable condensate would extend to several days. To overcome this, the reference hygrometer flushes the mirror with ambient air at the start of the measurement and only from condensation temperatures below −50 °C, causing immediate condensation of ambient humidity as ice on the chilled mirror surface. Further, the instrument monitors the resulting ice layer, and regulation is achieved by maintaining a steady state in which the ice layer thickness remains constant (phase boundary between solid and gas phase). If any organic compound were to condense onto the ice layer, the resulting change in the systems balance would be substantial. This would cause a huge rise in the mirror temperature, typically to around −40 °C or higher, since the measurement principle in this trace-level humidity range is extremely sensitive. Moreover, any organic compound capable of condensing under these conditions would have a condensation point significantly above −40 °C (e.g.: methylamine condenses at −17 °C). If such a compound did condense on the mirror, the mirror temperature would stabilize at that compound's condensation point. However, no such behaviour was observed, indicating that the water vapor measurement was entirely free from interference by any volatile degradation products of the MHP.

Figure S17 shows the emission of embedded water in an IBC solar cell. The trace humidity level prior to the emission was restored after approximately 80 minutes. The evaporated mass of water was calculated with the following equation:

$$\Delta m = \frac{M \cdot q_V \cdot \Delta t}{R \cdot T \cdot Z(p,T)_w} \cdot \sum_{i=1}^{n} e_w(IBC) \qquad (1)$$

Here, M is the molar mass of water with 0.0180153 kg/mol, q_V is the flow rate with 0.003 m³/min, Δt is the data logging interval of the transfer standard dew point hygrometer with 1/6 minutes (10 seconds), R is the universal gas constant with 8.314462 J/(mol · K), T is the absolute Temperature with 294.15 K, $Z(p,T)_w$ is the compressibility factor of humidity with 0.9456 at 1.0059 bar(a) and $e_w(IBC)$ is the water vapor partial pressure that outgassed from the IBC solar cell in Pa. Note that the measured frost point temperature is direct proportional to the water vapor partial pressure, using the state of the art ITS-90 Sonntag[1] equation. The emission was determined with a linear baseline at constant 0.1775 Pa ($e_w(i)_0$) from the process time of 01:57 to 03:16 (time required to return to the initial value before outgassing). Therefore, the emission from the IBC solar cell was calculated as following for the corresponding time stamp:

$$e_w(IBC) = e_w(i) - e_w(i)_0 \qquad (2)$$

with $e_w(i)$ being the measured water vapor partial pressure by the reference dew point hygrometer. It results a calculated emission of approximately 8.70 µg water in the form of humidity.

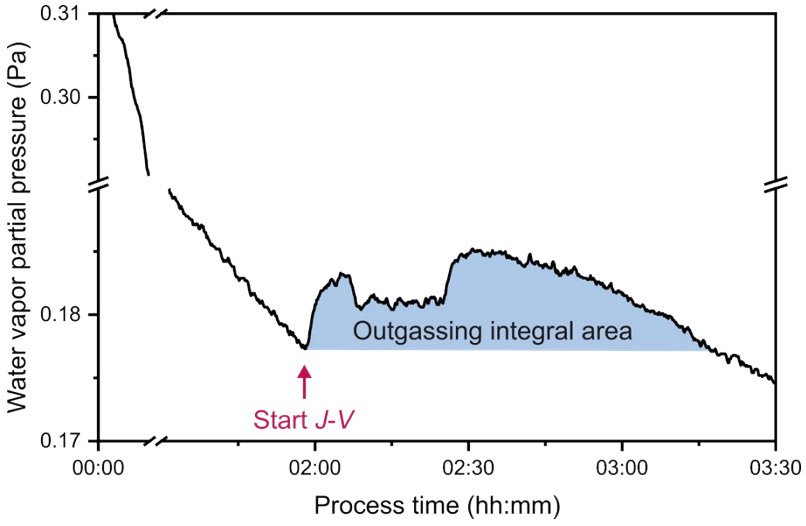

Figure S17: Observation of water outgassing with the onset of J-V pretreatments as preconditioning procedure to build up photocurrent and photovoltage. The outgassing integral area is shown in blue.

4.1 Calculation of the MHP mass on the active area

Based on literature data of the single perovskite densities and their mixing ratios, an estimated MHP density of 4.005 g/cm^3 was calculated (density of $MAPbBr_3$ = 3.582 g/cm^3, $FAPbI_3$ = 4.101 g/cm^3, α-$CsPbI_3$ = 4.811 g/cm^3 and $CsPbBr_3$ = 4.840 g/cm^3).[2-5]

Using this calculated MHP-density and by considering an active area of 0.260 cm^2 with a MHP layer thickness of 250 nm, the deposited mass on the active areas was calculated to be approximately 26 µg.

5. Trace humidity sample gases and parameter overview

Table S1: An overview of all significant trace humidity parameters for each humidified phase investigated. Standard deviations (SD) are listed with an expansion factor of 95 % (k = 2).

Humidification phase	t_f (°C)	SD	p_L (Pa)	SD	T (°C)	SD	Φ_w (ppm$_V$)	SD	$e_w(i)$ (Pa)	SD	$B'(T)$ (10^{-5} kPa^{-1})	$Z(p,T)_w$	c (µmol/L)
1	−65.70	0.25	100029.1	25.9	20.96	0.11	4.92	0.18	0.49	0.01	−54.103	0.9459	0.21183
2	−63.53	0.08	99812.6	41.0	20.96	0.09	6.70	0.08	0.66	0.01	−54.103	0.9460	0.28528
3	−61.88	0.29	99525.7	41.6	20.99	0.12	8.45	0.34	0.84	0.02	−54.065	0.9462	0.36301
4	−59.41	0.04	99182.2	64.4	21.01	0.12	11.86	0.07	1.17	0.01	−54.039	0.9464	0.50551
5	−56.75	0.10	99017.5	12.0	20.97	0.11	16.93	0.24	1.67	0.01	−54.090	0.9464	0.72151
6	−53.59	0.02	99058.3	11.9	20.98	0.12	25.47	0.07	2.51	0.01	−54.077	0.9464	1.08444
7	−51.31	0.03	99099.5	11.4	20.99	0.11	33.91	0.13	3.34	0.01	−54.065	0.9464	1.44305
8	−53.54	0.04	99221.0	13.6	20.99	0.11	25.58	0.14	2.52	0.01	−54.065	0.9464	1.08885
9	−56.64	0.06	99413.2	35.7	20.96	0.09	17.10	0.12	1.69	0.01	−54.103	0.9462	0.73033
10	−59.39	0.06	99696.7	40.5	20.98	0.10	11.84	0.10	1.17	0.01	−54.077	0.9461	0.50568
11	−61.98	0.12	100134.0	49.8	20.97	0.10	8.28	0.14	0.82	0.01	−54.090	0.9458	0.35450
12	−63.80	0.10	100546.2	41.7	20.97	0.11	6.41	0.09	0.64	0.01	−54.090	0.9456	0.27675
13	−66.18	0.20	100964.9	58.8	20.96	0.11	4.55	0.13	0.46	0.01	−54.103	0.9454	0.19896

The compressibility factors were calculated according to ISO 14912:2025[6] using the virial equation:

$$Z(p,T) = 1 + B'(T) \cdot p \quad (3)$$

Here, $B'(T)$ is the virial coefficient in Pa^{-1} and p the pressure in Pa. In the temperature range between 0 °C and 30 °C, the virial coefficient can be calculated approximately by linear interpolation:

$$B'(T) \approx B'_0 + (B'_{30} - B'_0)\frac{T(°C)}{30} \quad (4)$$

$T(°C)$ is the temperature in °C, B'_0 the second pressure-virial coefficient at 0 °C and B'_{30} the second pressure-virial coefficient at 30 °C.

The trace humidity concentrations $c(H_2O_{(g)})$ were calculated with the following equation:

$$c(H_2O_{(g)}) = \frac{e_w(i)}{R \cdot T \cdot Z(p,T)_w} \quad (5)$$

6. Baseline correction methodology & quenching ratio determination

To correct the non-linear baseline drift of the current density during long-term measurements, a baseline correction procedure was applied. A series of anchor points was defined at positions where the current density under dry conditions exhibited a stable and uniform slope. In addition, anchor points following trace humidity exposure were defined at least 20 min after completion of each stage in order to capture the intrinsic recovery behaviour of the current density signal, with typically 4 to 6 anchor points placed between successive humidity injections. The baseline between adjacent anchor points was determined by linear interpolation. Consequently, for each trace humidity measurement, the local baseline was defined by the anchor points immediately before and after the respective humidity level and linear interpolation. In this way, the overall non-linear baseline drift was represented by a sequence of linear segments connecting successive anchor points.

This procedure is further illustrated in **Figure S18**. **Figure S18a** shows an enlarged section of the current density dataset, in which the trace humidity injections are clearly resolved as distinct and well-defined events. **Figure S18b** shows the corresponding baseline reconstruction for two representative events. The baseline (blue line) is in very good agreement with the measured signal under dry conditions.

As illustrated in **Figure S18c**, the Stern-Volmer current density ratios were extracted from these data and are listed in **Table S2**. The value of J is determined as the local minimum of the signal,

corresponding to the point of maximum charge-carrier quenching. The corresponding *x*-coordinate of maximum charge-carrier quenching is then used to determine the *y*-value of the baseline at the same position. This yields an estimate (by linear extrapolation) of the current density signal that would be expected in the absence of the quencher. As a result, degradation-related contributions can be removed from the charge-carrier quenching ratios, allowing the pure water-induced effect to be isolated.

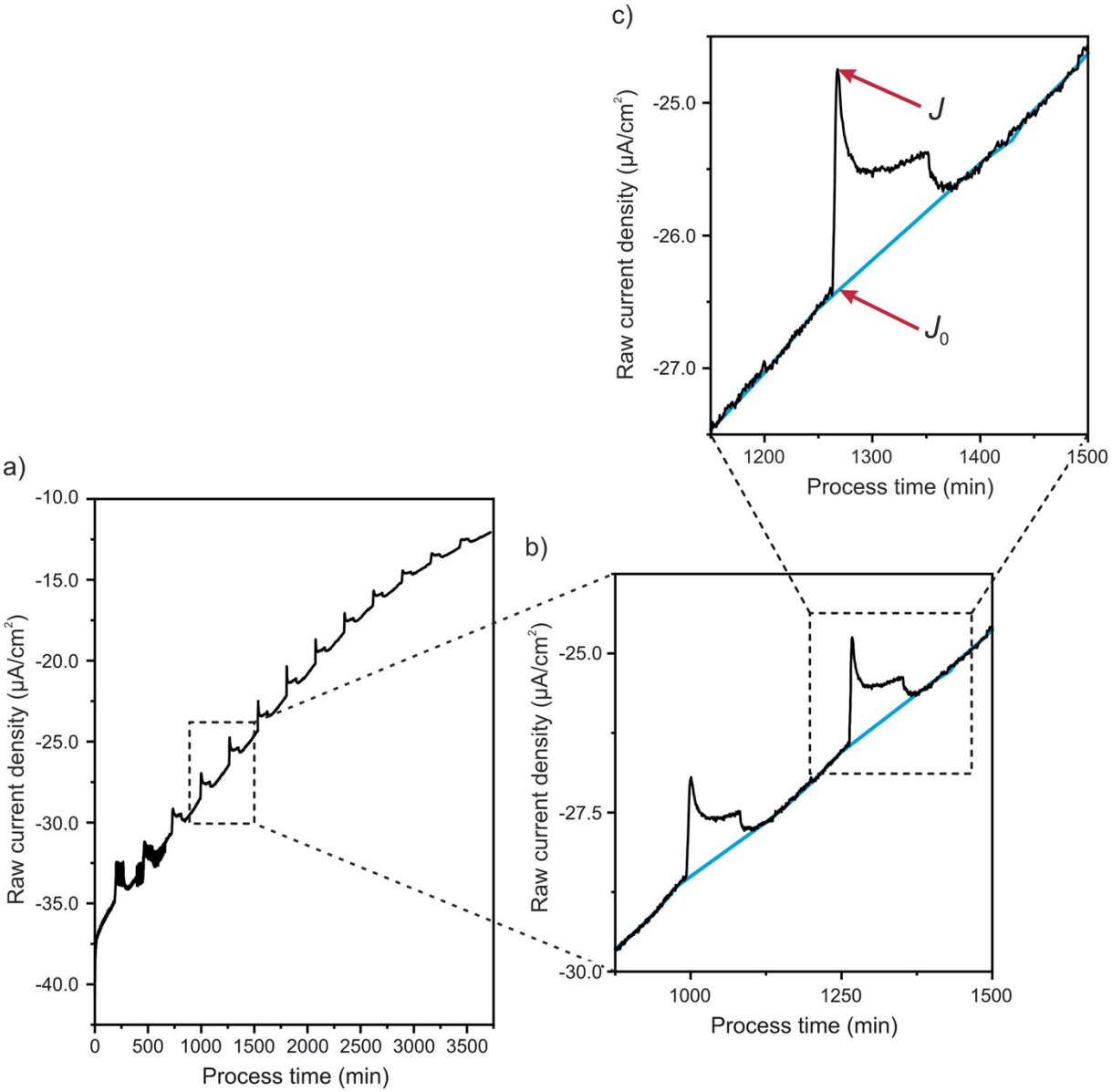

Figure S18: *Illustration of the baseline correction procedure used for the determination of SV charge-carrier quenching ratios. a) Raw current density signal measured during long-term trace humidity measurements, showing a slow baseline drift with distinct humidity-induced quenching events. b) Enlarged section of the dataset and the reconstructed baseline (blue line) obtained by linear interpolation between anchor points. c) Example of the extraction procedure for the SV ratio.*

Table S2: List of the maximum quenched current density, the baseline current density and the amount of trace humidity of the corresponding humidification phase.

Increasing Amounts of Trace Humidity					Decreasing Amounts of Trace Humidity				
Volume Fraction (ppm_V)		Raw Current Density ($\mu A/cm^2$)		$\frac{J_0}{J}$	Volume Fraction (ppm_V)		Raw Current Density ($\mu A/cm^2$)		$\frac{J_0}{J}$
	SD	J	J_0			SD	J	J_0	
4.92	0.18	−33.95	−34.95	1.0295	33.91	0.13	−20.34	−22.16	1.0895
6.70	0.08	−31.62	−33.41	1.0566	25.58	0.14	−18.68	−20.17	1.0798
8.45	0.34	−29.15	−30.54	1.0477	17.10	0.12	−17.06	−18.25	1.0698
11.86	0.07	−26.95	−28.50	1.0575	11.84	0.10	−15.67	−16.58	1.0581
16.93	0.24	−24.75	−26.42	1.0675	8.28	0.14	−14.43	−15.12	1.0478
25.47	0.07	−22.49	−24.30	1.0805	6.41	0.09	−13.35	−13.93	1.0434
33.91	0.13	−20.34	−22.16	1.0895	4.55	0.13	−12.52	−12.95	1.0343

Nomenclature

J	Current density
V	Voltage
J_{SC}	Short-circuit current density
V_{OC}	Open-circuit voltage
Δm	Mass difference
q_V	Flow rate
Δt	Time interval of data logging
M	Molar mass
R	Universal gas constant
T	Temperature
$Z(p,T)$	Compressibility factor
$e_w(IBC)$	Water vapor partial pressure emitted from the IBC solar cell
$e_w(i)$	Water vapor partial pressure
$e_w(i)_0$	Water vapor partial pressure before outgassing
t_f	Frost point temperatures
p_L	Absolut pipe pressure
Φ_w	Humidity volume fractions
$B'(T)$	Virial coefficient
$Z(p,T)_w$	Compressibility factor of water vapor
c	Concentration
k	Expansion factor
SD	Standard deviation
U	Uncertainty
p	Pressure
B_0'	The second pressure-virial coefficient at 0 °C
B_{30}'	The second pressure-virial coefficient at 30 °C
$T(°C)$	Temperature in °C
J_0	Current density in the absence of the quencher

References

1. D. Sonntag, *Zeitschrift für Meteorologie*, 1990, **70**, 340–344.
2. C. C. Stoumpos, C. D. Malliakas and M. G. Kanatzidis, *Inorganic Chemistry*, 2013, **52**, 9019–9038.
3. M. I. Saidaminov, A. L. Abdelhady, B. Murali, E. Alarousu, V. M. Burlakov, W. Peng, I. Dursun, L. Wang, Y. He, G. Maculan, A. Goriely, T. Wu, O. F. Mohammed and O. M. Bakr, *Nature Communications*, 2015, **6**, 7586.
4. B. Wang, N. Novendra and A. Navrotsky, *Journal of the American Chemical Society*, 2019, **141**, 14501–14504.
5. M. Zhang, Z. Zheng, Q. Fu, Z. Chen, J. He, S. Zhang, L. Yan, Y. Hu and W. Luo, *CrystEngComm*, 2017, **19**, 6797–6803.
6. ISO 14912:2025, *Gas analysis – Conversion of gas mixture composition data*, International Organization for Standardization, Geneva, 2025.